Matthew Emes, Azadeh Jafari, Maziar Arjomandi
Wind load design considerations for the elevation and azimuth drives of a heliostat
Proceedings of the 25th Solar Power and Chemical Energy Systems Annual Conference (SolarPACES 2019), as published in AIP Conference Proceedings, 2019 / vol.2303, pp.030013-1-030013-1-10

Wind Load Design Considerations for the Elevation and Azimuth Drives of a Heliostat

Matthew Emes,[1, a)] Azadeh Jafari,[1, b)] Maziar Arjomandi [1, c)]

[1] *Centre for Energy Technology, School of Mechanical Engineering, University of Adelaide, Adelaide, SA 5005, Australia*

[a)] Corresponding author: matthew.emes@adelaide.edu.au
[b)] azadeh.jafari@adelaide.edu.au
[c)] maziar.arjomandi@adelaide.edu.au

Abstract. This paper investigated the dynamic fluctuations of the high-frequency surface pressure and force measurements on an instrumented scale-model heliostat within a turbulent ABL generated in a wind tunnel. Peak aerodynamic load coefficients on the model heliostat calculated following the equivalent static wind load method were consistent with previous wind tunnel studies in the literature. The dynamic analysis of the hinge, azimuth and overturning moments in the current study showed that there are a range of critical load cases and heliostat configurations that need to be considered to investigate the dynamic loading on the elevation and azimuth drives of a heliostat. Quasi-steady variation of the fluctuating peak loads following a Gaussian distribution was found to under-predict the maximum hinge and overturning moments in operating and stow configurations. It is therefore recommended that the analysis of instantaneous loads on the elevation drive and pedestal foundation is carried out for an improved estimation of the heliostat design wind loads.

INTRODUCTION

Unsteady pressure distributions and forces on heliostats are induced by turbulent fluctuations in the lower surface layer of the atmospheric boundary layer (ABL) at heights below 20 m. The structural stiffness and strength of individual heliostats need to be maintained throughout a typical 30-year working life of a central receiver field, through consideration of the maximum wind loading and the subsequent sizing of the wind-bearing components in the heliostat design. Peterka and Derickson [1] reported the mean and peak aerodynamic coefficients of the hinge moment M_{Hy} about the central elevation y_H-axis of the heliostat, the azimuth moment M_z about the vertical z-axis and the overturning moment M_y about the y_b-axis at the base of heliostat pedestal (Figure 1b). The aerodynamic coefficients were calculated following quasi-static theory applied to high-frequency force balance measurements in simulated ABL wind tunnel experiments and the mean wind speed at the elevation axis height of a scale-model heliostat. The equivalent static wind loads on heliostats following the design codes and provisions for buildings are based on extreme value analysis that the three-sigma peak aerodynamic coefficients have a 99.7% probability of not being exceeded [2]. Experimental studies in the literature have primarily focused on the equivalent static wind loads on heliostats over a range of elevation and azimuth angles, however the dynamic characteristics of the critical load cases on heliostats are most relevant for the sizing of the heliostat drive units. The high-amplitude gust loading on the azimuth and elevation drives of the Sandia heliostat at the National Solar Thermal Test Facility (NSTTF) by Ho *et al.* [3] was found to be most significant for fatigue and durability considerations, corresponding to the low-frequency (1-2 Hz) turbulent fluctuations in the ABL that are close to the frequency range of the structural modes of vibration. Pfahl *et al.* [4] showed that the maximum hinge moment coefficients calculated using field measurements on a heliostat in stow position instrumented with 84 differential pressure sensors were of a short duration of the

order of 0.7 seconds. This indicates that the 3-second gust wind speed following a quasi-steady approximation in design codes and standards for large physical structures, such as buildings in ASCE 7-02 [5] and AS/NZS 1170.2 [6], is likely to under-estimate the maximum loads on rooftop solar panels in ASCE/SEI 7-16 [7] and heliostats. The maximum loads on a heliostat in stow position are considered to be most important for design purposes due to the larger survival wind speed compared to the maximum operational wind speed, however the azimuth and overturning moments are significant during operation. Hence, the current study aims to determine the critical load cases corresponding to the maximum hinge and azimuth moments on a scale-model heliostat during operation and in stow position. The heliostat configurations for the maximum loads on the drive units and the pedestal foundation are identified through an investigation of the instantaneous pressure distributions on the heliostat surface and the instantaneous forces at the base of the heliostat within two simulated ABLs closely representing the full-scale velocity profiles and turbulence intensities over a flat "open country" terrain and a suburban terrain.

METHODOLOGY

The current study reports the dynamic pressure fluctuations derived from the peak instantaneous heliostat load measurements within two part-depth atmospheric boundary layers (ABLs). The boundary layers were generated using two different sets of truncated spires and a staggered arrangement of roughness elements within a test section of 3 m × 3 m cross-section and 17 m development length at the University of Adelaide wind tunnel. Mean velocity and turbulence intensity profiles closely represent ESDU 85020 [8] profiles at the position of the instrumented heliostat model in Figure 1a with constant elevation axis height $H = 0.5$ m and chord length $c = 0.8$ m [9]. The mean velocity profiles of the two simulated ABLs are shown by Jafari *et al.* [2] to approximate a logarithmic profile corresponding to a flat "open country" terrain ($z_0 = 0.018$ m) and a suburban terrain ($z_0 = 0.35$ m in Figure 1a) at measurement heights 0.15 m $\leq z \leq$ 0.65 m. Jafari *et al.* [2] showed that the turbulence intensities in the longitudinal direction $I_u = \sigma_u/U$ (13% and 26%) and vertical direction $I_w = \sigma_w/U$ (9% and 11%) in the two simulated ABLs are within the allowable bandwidth of ±20% from the predicted values in ESDU 85020 [8]. Further detail of the velocity and turbulence intensity profiles and a discussion of the differences between the longitudinal and vertical velocity spectra and turbulence length scales in the wind tunnel and atmosphere are provided in Jafari *et al.* [2, 10]. For the analysis of dynamic wind loads in the current study, the mean velocity and turbulence intensity at the elevation axis height of the instrumented heliostat model is considered appropriate for comparison of the aerodynamic peak coefficients with those in the literature at similar turbulence intensities.

The experimental velocity and force measurement devices were set up in the wind tunnel for high-frequency sampling at 1 kHz to sufficiently resolve the fluctuating components of the turbulent flow and the aerodynamic loads, respectively. Three velocity components of the turbulent flow approaching the heliostat were measured at the tunnel centerline using a multi-hole pressure probe and vertical profiles were obtained using a two-dimensional traverse system. The elevation angle (α) of the heliostat surface with respect to the horizontal was varied in increments of 15° between 0° and 90° using a hinge pin joint between the heliostat facet and the pylon. The azimuth angle (β) was varied in increments of 30° between 0° and 180° using a turntable. Differential pressures were obtained between the taps on the upper and lower surfaces of the heliostat facet connected by tubes to the pressure sensors inside the heliostat cavity. Forces at the base of the heliostat model using four three-axis load cells mounted at the corners of a force balance and turntable support structure. Hinge moments on the heliostat were calculated from the weighted summation of the measured surface pressures as the product of the normal force and the distance to the centre of pressure from the central elevation (y_H) axis of the heliostat [11]. Azimuth and overturning moments on the heliostat were calculated using the summation of forces in the three Cartesian directions (x, y, z) measured by the load cells in the base balance. The peak load coefficients on the heliostat were estimated as the sum of the mean values and three times the standard deviation of the fluctuating load measurements, following the quasi-steady approximation and a Gaussian distribution with a 99.7% probability of not being exceeded [1, 12].

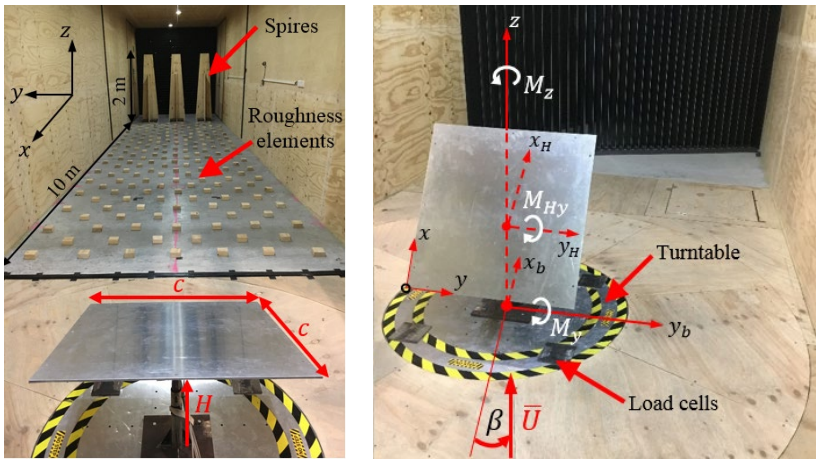

(a) (b)

FIGURE 1. Experimental setup in the University of Adelaide wind tunnel for (a) generation of the mean velocity and turbulence intensity profiles in the lowest 120 m of the atmospheric boundary layer, and (b) high-frequency surface pressure and force measurements on a model heliostat with $c = 0.8$ m and $H = 0.5$ m.

RESULTS AND DISCUSSION

Figure 2 shows the peak hinge and azimuth moment coefficients calculated as a function of elevation angle α and azimuth angle β in a simulated wind tunnel boundary layer with mean velocity $\overline{U} = 8.4$ m/s and turbulence intensity $I_u = 13\%$ at the elevation axis (hinge) height of the heliostat. The hinge and azimuth moment coefficients were calculated using the fluctuating pressure and force measurements on the instrumented heliostat, respectively, following the equations in Peterka and Derickson [1]. The hinge moment coefficients are highly dependent on α due to the increased movement of the centre of pressure towards the windward edge of the heliostat as α approaches 0° (stow position) and β approaches 0° and 180° [13]. The maximum (positive clockwise rotation about the y_H axis in Figure 1b) and minimum (negative anti-clockwise rotation about the y_H axis in Figure 1b) hinge moment coefficients of 0.20 and -0.21 at $\beta = 0°$ and 180°, respectively, correspond to the maximum lift force at $\alpha = 30°$. In contrast, the azimuth moment coefficients are dependent on the azimuth angle, with maximum and minimum values at $\beta = 60°$ and 120°, corresponding to the maximum drag force on a heliostat at $\alpha = 90°$. The maximum and minimum overturning moment coefficients about the y_b axis at the base of the heliostat also occur at $\alpha = 90°$ and $\beta = 0°$ and 180°, respectively, with the maximum projected frontal area of the heliostat to the approaching wind.

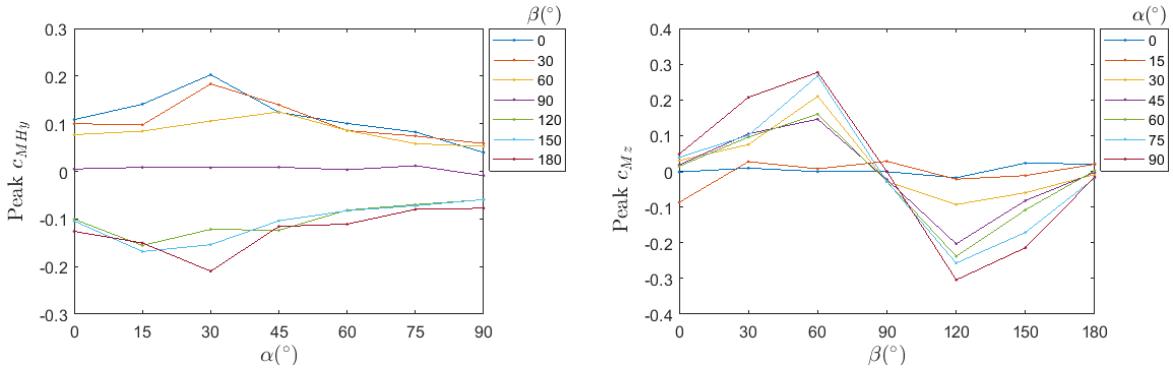

(a) (b)

FIGURE 2. Variation of peak aerodynamic load coefficients with heliostat elevation angle α and azimuth angle β at $I_u = 13\%$: (a) hinge moment M_{Hy}, (b) azimuth moment M_z.

Table 1 presents the critical load cases corresponding to the maximum and minimum hinge, azimuth and overturning moment coefficients in a moderate $I_u = 13\%$ representative of a flat open country terrain and a high $I_u = 26\%$ corresponding to a suburban terrain. The values of the peak moment coefficients increase significantly with increasing I_u following the findings of Peterka *et al.* [14]. The peak moment coefficients calculated using the three-sigma approach in the current study at $I_u = 13\%$ are comparable with previous experimental studies [1, 14, 15] on heliostats at similar turbulence intensities. Due to the negligible difference in the magnitudes of the peak hinge, azimuth and overturning moment coefficients at $\beta = 0°$ and 180°, the dynamic analysis of the loads in the following results is concentrated on the maximum (positive) cases at $I_u = 13\%$ in Table 1. Furthermore, the moderate turbulence case in the current study closely represents the velocity and turbulence characteristics during high-wind periods over an "open country" terrain surrounding a heliostat field [10].

TABLE 1. Critical load cases of a model heliostat in two simulated atmospheric boundary layers corresponding to the maximum and minimum aerodynamic coefficients.

Critical load case	**Heliostat component**	**Load coefficients**		**Elevation angle** $\boldsymbol{\alpha}$ (°)	**Azimuth angle** $\boldsymbol{\beta}$ (°)
		$\boldsymbol{I_u = 13\%}$	$\boldsymbol{I_u = 26\%}$		
Hinge moment	Elevation drive	0.20	0.65	30	0
M_{Hy}		-0.21	-0.76	30	180
Azimuth moment	Azimuth drive	0.28	1.08	90	60
M_z		-0.30	-1.02	90	120
Overturning moment	Foundation	2.29	5.33	90	0
M_y		-2.06	-4.33	90	180
Stow position	Elevation drive,	0.11, 0.43	0.45, 1.18	0	0
M_{Hy}, M_y	foundation	-0.13, -0.35	-0.37, -0.98	0	180

Figure 3 shows the instantaneous pressure coefficient distributions on the heliostat surface corresponding to the azimuth-elevation configurations of the maximum hinge and azimuth moments. The high-pressure region is concentrated over the windward half of the heliostat at the instant of the maximum hinge moment $c_{MHy} = 0.18$ (Figure 3a) on the operating heliostat. The heliostat configuration of $\alpha = 30°$ and $\beta = 0°$ corresponds to the maximum lift coefficient $c_{Fz} = 2.83$ and a longitudinal movement of the centre of pressure of 0.09 m toward the leading edge ($x = 0$ m) from the central elevation axis ($x = 0.4$ m). Despite a smaller lift force $c_{Fz} = 0.42$ on the stowed heliostat at $\alpha = 0°$, the increased longitudinal movement of the centre of pressure of 0.1 m from the central elevation axis ($x = 0.4$ m) in the instantaneous distribution in Figure 3b leads to the maximum hinge moment on the heliostat in stow position. Hence, the maximum loads on the elevation drive are caused by the concentrated region of high pressure on the frontal half of the heliostat surface during operation ($\alpha = 30°$) and the build-up of pressure along the windward edge of the heliostat surface in stow position ($\alpha = 0°$). In contrast, the maximum azimuth moment during operation in Figure 3c corresponds to the maximum drag coefficient $c_{Fx} = 2.29$ on the heliostat in vertical position ($\alpha = 90°$) with wind approaching the heliostat at $\beta = 60°$. Hence, the maximum loads on the azimuth drive are caused by heliostat configurations corresponding to large drag forces and the maximum movement of the centre of pressure toward the side edges of the heliostat at $\beta = 60°$ and 120°.

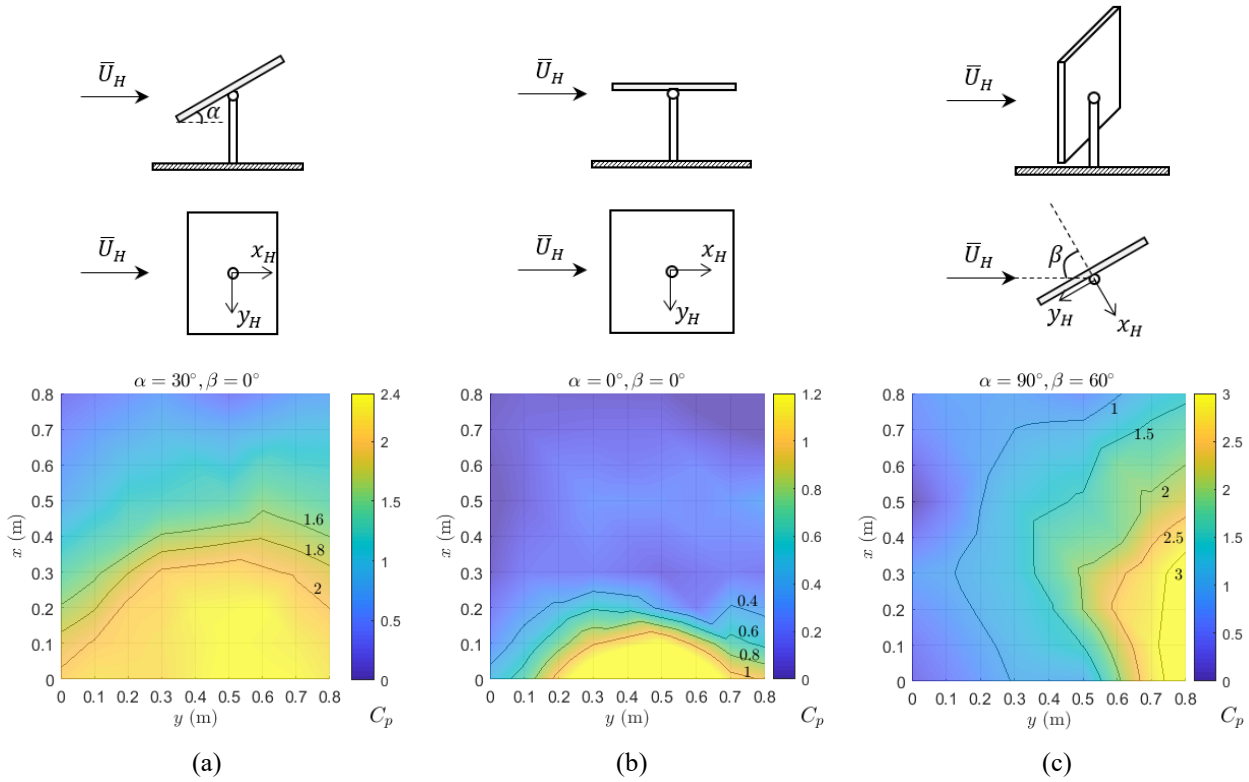

FIGURE 3. Side and plan views of the heliostat elevation-configurations and the instantaneous pressure coefficient distributions on the heliostat surface (x, y) at $I_u = 13\%$ corresponding to the maximum: (a) hinge moment during operation, (b) hinge moment in stow position, (c) azimuth moment during operation.

Figure 4 shows the power spectra or Fast Fourier Transform (FFT) of the fluctuating differential pressure signals measured at different longitudinal points along the heliostat surface (x, y) near the centreline at $y = 0.5$ m. The pressure fluctuations on the heliostat surface corresponding to the largest spectral energies $S_p > 10$ Pa^2/Hz are concentrated at frequencies f below 5 Hz for the maximum hinge and azimuth moments. The peak spectral energy corresponding to the maximum operating hinge moment (Figure 4a) of $S_p = 52.2$ Pa^2/Hz occurs at $f = 0.24$ Hz near the leading edge at $x = 0.1$ m. There is a secondary peak $S_p = 50.5$ Pa^2/Hz at $f = 2.2$ Hz on the heliostat surface at $x = 0.3$ m, which more closely corresponds to the peak spectral energies $S_p > 50$ Pa^2/Hz at $f = 1.2$ Hz and 3.4 Hz on the heliostat configuration for the maximum azimuth moment in Figure 4c. The vortex shedding on the heliostat for these cases may present a significant wind load fluctuation associated with pronounced vibration and resonance effects on the elevation and azimuth drives in the typical 2-5 Hz range of natural frequencies of a conventional heliostat [16, 17]. In contrast in stow position (Figure 4b), the maximum energy of the pressure fluctuations $S_p = 28.39$ Pa^2/Hz at the position (0.1 m, 0.5 m) near the leading edge of the heliostat surface is approximately half of the peak magnitudes during operation in Figure 4a. Furthermore, the peak spectral energy of the pressure fluctuations at downstream x-positions on the stowed heliostat surface are an order of magnitude smaller than the maximum values at $x = 0.1$ m near the leading edge. Hence, the significant increase in the magnitudes of the fluctuating pressures toward the leading edge in Figure 4b shows that the maximum hinge moment about the central elevation axis in stow position is a critical load case for dimensioning of the elevation drive.

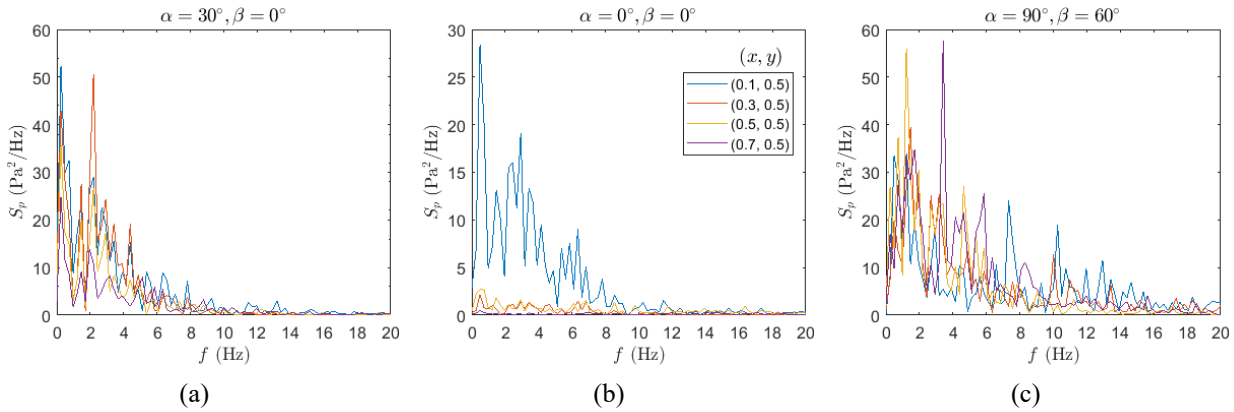

FIGURE 4. Power spectra of the pressure fluctuations at $y = 0.5$ m near the centerline of the heliostat surface (x, y) at $I_u = 13\%$ corresponding to the maximum: (a) hinge moment, (b) hinge moment in stow position, (c) azimuth moment.

Figure 5 presents the time-varying load coefficients for the hinge, azimuth and overturning moments on the heliostat corresponding to the maximum operating and stow configurations in Table 1. It can be observed that the load coefficients in stow position have near-zero mean values but a significant fluctuating component due to the turbulent fluctuations of the approaching ABL with $\overline{\overline{U}} = 8.4$ m/s and $I_u = 13\%$ at the heliostat elevation axis height $H = 0.5$ m. The magnitudes of the hinge moment coefficient in stow position (Figure 5a) are smaller than the field measurements by Pfahl *et al.* [4] on an isolated 8 m^2 heliostat instrumented with 84 differential pressure sensors in Lilienthal, Germany. The reason for the differences in the hinge moment coefficients is likely to be the larger turbulence intensities and length scales in the full-scale ABL at the smaller mean wind speed $\overline{U}_H = 5.5$ m/s during the field measurements [4]. The azimuth and overturning moment coefficients in Figure 5b and Figure 5c, respectively, show reasonable agreement with the mean and peak coefficients reported by Peterka *et al.* [14, 18] at similar turbulence intensities (I_u) to the current study. It can be seen that the maximum load coefficients, particularly in stow position, in most cases exceed the defined peak coefficient. The maximum loading cases are therefore highly dependent on the turbulence flow characteristics of the terrain features surrounding a heliostat field site. Figure 5 shows that there are distinctive frequencies and amplitudes corresponding to the maximum load fluctuations for each of the critical loading cases, such that the heliostat design of individual heliostat components should be considered independently. It is noted that the operating and stow load coefficients in the current study are all calculated in a simulated ABL with mean velocity $\overline{U} = 8.4$ m/s at the heliostat elevation axis (hinge) height. Despite the smaller load coefficients in stow position, the design loads on the stowed heliostat need to consider that the maximum survival wind speed is considerably larger than the maximum operational wind speed.

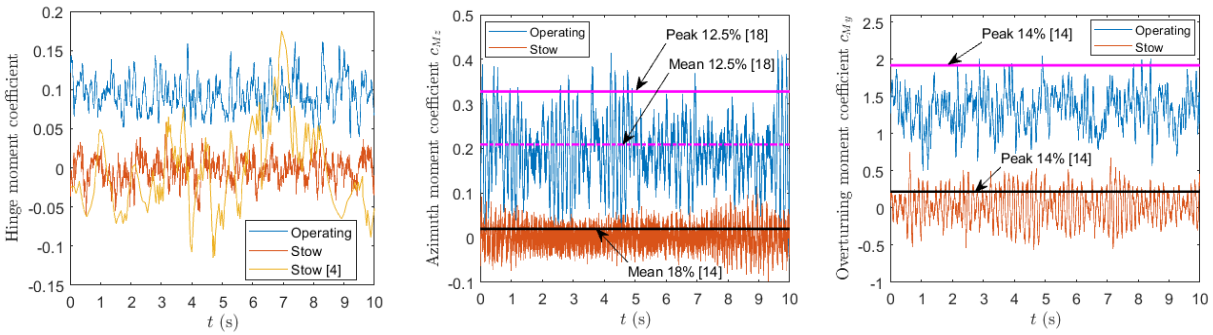

FIGURE 5. Time-varying load coefficients on the heliostat during the maximum operating and stow configurations from Table 1 at $I_u = 13\%$: (a) hinge moment c_{MHy}, (b) azimuth moment c_{Mz}, (c) overturning moment c_{My}. The magenta and black horizontal

lines represent the heliostat load coefficients during operating and stow configurations, respectively, at different I_u reported by Peterka *et al* [14, 18]. The yellow line in Figure 5a indicates the time-varying hinge moment coefficient reported by Pfahl *et al.* [4] during field measurements on an 8 m^2 heliostat in Lilienthal, Germany.

Figure 6 shows the power spectra (FFT) of the transient heliostat load coefficients of the hinge, azimuth and overturning moments for the maximum operating and stow configurations in Figure 5. The hinge moment spectra in Figure 6a closely resemble the spectra of the velocity measurements in the flow with an approximately constant maximum energy in the low-frequency range (1 Hz $\leq f \leq$ 10 Hz) and a linear variation of the spectral distribution in the mid-frequency range (10 Hz $\leq f \leq$ 50 Hz). Furthermore, the maximum energy of the hinge moment fluctuations in the maximum operating case ($\alpha = 30°$) is three orders of magnitude larger than those in the stow position. In contrast, there is a clearly defined peak of the azimuth moment spectra and overturning moment spectra at $f \approx 7$ Hz in the maximum operating and stow cases in Figure 6b and Figure 6c, respectively. The peak spectral energy in the maximum operating azimuth case is more than an order of magnitude larger than those at $f \leq 5$ Hz and $f \geq 10$ Hz. There is a secondary peak of the azimuth and overturning moment spectral distributions, that is most pronounced in stow position, at $f = 12.7$ Hz and 18.1 Hz, respectively. In comparison, a Large Eddy Simulation (LES) by Vásquez-Arango [19] found a pronounced peak at $f = 3.8$ Hz in the spectral distribution of the overturning moment coefficients on a 2.5 m × 3.22 m heliostat model. In a field experiment study at Sandia National Laboratories, Ho *et al.* [20] reported two low-frequency rigid-body modes of vibration of the full-scale 37 m^2 NSTTF heliostat at 1-2 Hz caused by backlash of the elevation and azimuth drive motors [17, 20]. The modal frequencies of the NSTTF heliostat were found to be largely dependent on the heliostat size, such that the azimuth drive modal frequency increased from 1.28 Hz to 2.28 Hz at $\alpha = 90°$ and from 1.04 Hz to 1.75 Hz at $\alpha = 0°$ with increasing heliostat size from 37 m^2 to 60 m^2 [20]. To prevent the overloading of the elevation and azimuth drives and preserve the torsional rigidity of the heliostat pedestal, the modal frequencies of the structure need to be avoided through consideration of the sizing of heliostat components with respect to the load fluctuations induced by turbulence in the ABL. This is beyond the scope of the current study, and would require additional detailed measurements of the vibrational response and mode shapes of the instrumented heliostat.

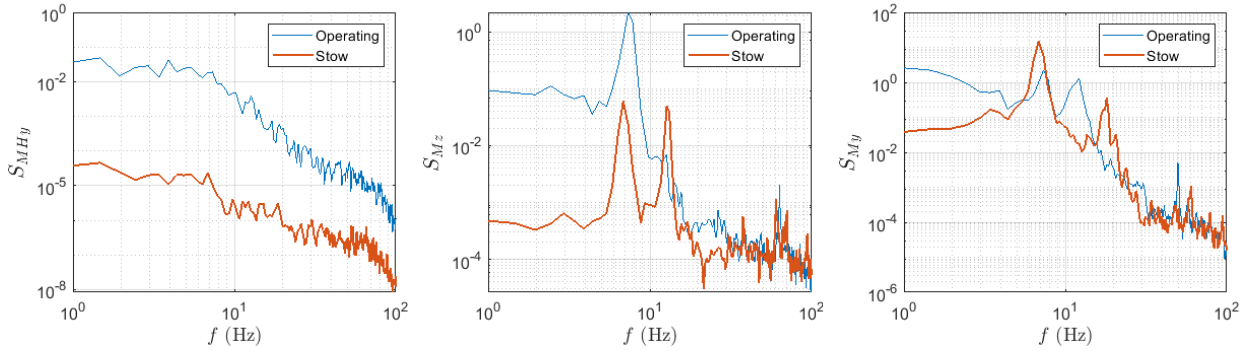

FIGURE 6. Power spectral density of the fluctuating loads on the heliostat during the maximum operating and stow configurations from Table 1 at $I_u = 13\%$: (a) hinge moment, (b) azimuth moment, (c) overturning moment.

Figure 7 presents the probability distributions of the fluctuating moment coefficients on a heliostat in the maximum operating and stow load configurations, compared to a fitted normal distribution with the defined parameters in Table 2. The operating (Figure 7c) and stow (Figure 7d) azimuth moment coefficients are most accurately represented by a normal distribution with $R^2 > 0.97$ and root-mean-square-error ($RMSE$) ≤ 0.0031, compared with $R^2 < 0.97$ and $RMSE \geq 0.0035$ for the hinge moment and overturning moment coefficients. The hinge moment coefficients exhibit a positively skewed distribution, such that the probability of the largest values of

the operating coefficients ($c_{MHy} > 0.31$ in Figure 7a) and stow coefficients ($c_{MHy} > 0.05$ in Figure 7b) are under-predicted by as much four times by a normal distribution. Similarly, the upper end of the operating (Figure 7e) and stow (Figure 7f) overturning moments are poorly predicted by a normal distribution. Quasi-steady theory assumes full correlation between the velocity and load correlations on heliostats in the wind load design method by Peterka and Derickson [1]. The results in Figure 7 and Table 2 suggest that assuming a quasi-steady variation of the fluctuating peak loads following a Gaussian distribution is reasonable to predict the maximum operational and stow azimuth load case. However, the dynamic analysis of the load fluctuations is recommended to complement the quasi-steady peak load coefficients to determine the critical load cases for the maximum hinge and overturning moments on a heliostat in response to ABL turbulence.

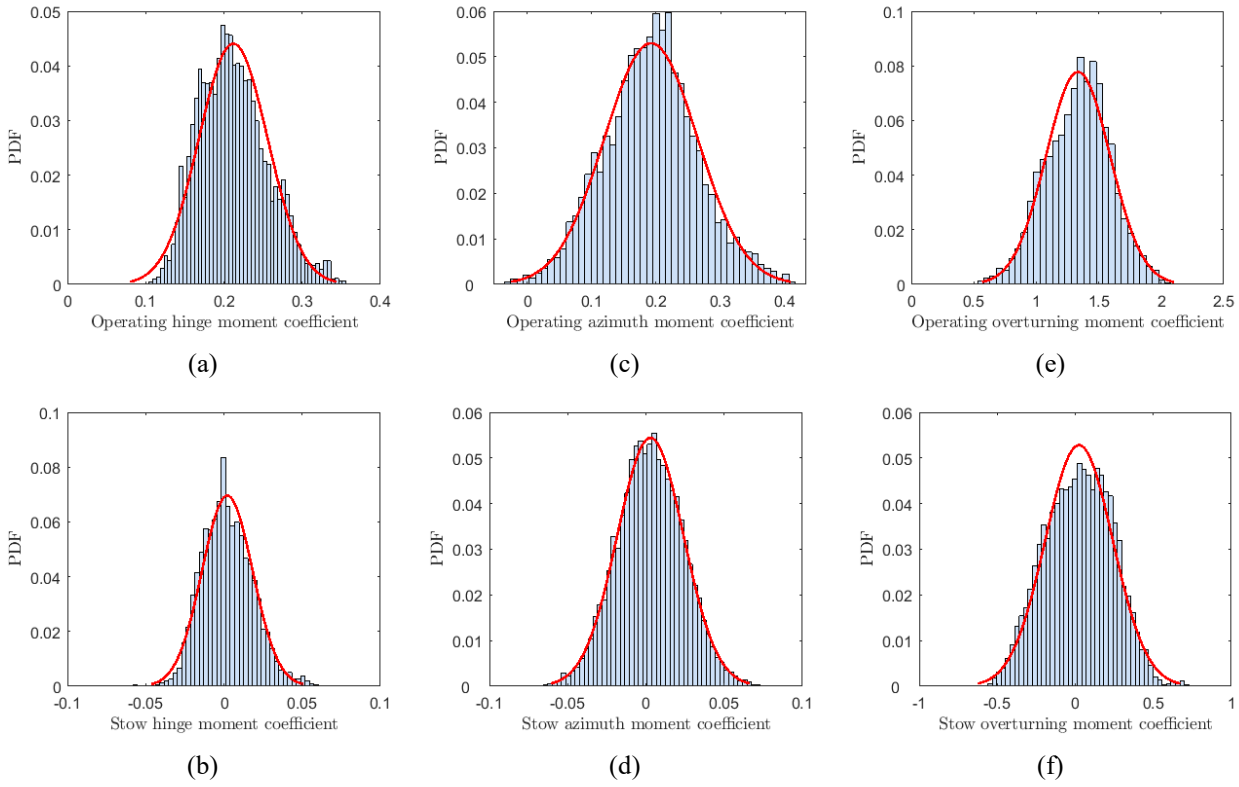

FIGURE 7. Probability distribution of the fluctuating heliostat load coefficients in Figure 5 compared with a fitted normal distribution (solid red line) corresponding to the heliostat configurations in Table 1 for the maximum: (a) operating hinge moment, (b) stow hinge moment, (c) operating azimuth moment, (d), stow azimuth moment, (e) operating overturning moment, (f) stow overturning moment.

TABLE 2. Probability distribution parameters for the critical load cases in Figure 7.

Heliostat component	Critical load case	Mean μ	Standard deviation σ	Skewness	Kurtosis	R^2	RMSE
M_{Hy}	Operating	0.212	0.044	0.31	1.60	0.9318	0.0041
Elevation drive	Stow	0.002	0.016	0.69	2.03	0.9678	0.0045
M_z	Operating	0.192	0.072	0.68	2.08	0.9741	0.0031
Azimuth drive	Stow	0.003	0.021	0.79	2.06	0.9934	0.0016
M_y	Operating	1.335	0.257	0.48	1.80	0.9610	0.0054
Foundation	Stow	0.024	0.216	0.17	1.41	0.9635	0.0035

CONCLUSIONS

This experimental study investigated the dynamic fluctuations of the high-frequency surface pressure and force measurements on an instrumented scale-model heliostat within a turbulent ABL generated in a wind tunnel. Peak aerodynamic load coefficients on the model heliostat show general agreement with previous wind tunnel studies in the literature at similar turbulence intensities, providing confidence in the dynamic analysis of the fluctuating loads on the heliostat components. The results show that there are a range of critical load cases and heliostat configurations that need to be considered to investigate the maximum loading on the elevation and azimuth drives of a heliostat:

- The maximum *hinge moment* about the elevation axis of a heliostat at $\alpha = 30°$ during operation is caused by the concentrated region of high pressure near the windward edge of the heliostat surface at $\beta = 0°$.
    - The peak of the spectral distribution of the pressure fluctuations in stow position is an order of magnitude larger near the leading edge than downwind points on the heliostat surface, and the peak spectral energy magnitude in stow is approximately half that during the maximum operating case.
    - The probability of the maximum operating and stow coefficients are under-predicted by as much four times by a normal distribution fitted to the hinge moment fluctuations.
- The maximum *azimuth moment* about the vertical axis of a heliostat corresponds to large drag forces in a vertical orientation ($\alpha = 90°$) and the maximum movement of the centre of pressure toward the side edges of the heliostat at $\beta = 60°$ and $120°$.
    - Spectral distribution of the load fluctuations shows a clearly defined peak at a frequency of 7 Hz that is close to the typical range of natural frequencies of a conventional heliostat.
    - The probability distribution of the maximum azimuth moments in operating and stow positions is well represented by a normal distribution with $R^2 > 0.97$ and $RMSE \leq 0.0031$.
- The maximum *overturning moment* about the base of the heliostat correlates closely to the maximum drag forces on a heliostat positioned normal to the ABL flow at $\alpha = 90°$ and $\beta = 0°$.
    - There is a clearly defined peak at a frequency of 7 Hz that can present a significant risk to the structural rigidity of the heliostat pedestal foundation during operation.
    - The probability of the maximum operating and stow coefficients are not well predicted by a normal distribution fitted to the overturning moment fluctuations.

The results indicate that the quasi-steady assumption of the fluctuating peak loads following a Gaussian distribution is generally appropriate to predict the maximum azimuth moments in operating and stow configurations. The assumption of the full correlation between the velocity and load correlations on heliostats adopted in the equivalent static wind load design methods by Peterka and Derickson [1] is inadequate for the maximum operating hinge and overturning moments on a heliostat. Dynamic analysis of the transient load fluctuations in these critical load cases is therefore recommended to more closely estimate the critical heliostat load cases, such as overload failures of the elevation drive and torsional rigidity of the pedestal, in response to turbulence in the ABL. It is acknowledged that the single turbulence case for dynamic analysis in the current study can be extended to additional turbulence characteristics and increased flow velocities to account for the maximum operational and stow survival wind speeds. The objective of future work is to apply the techniques to analyse field measurements on small-scale prototype heliostats for the critical load cases investigated in the current study. The results will form part of Heliostat Wind Load Design Guidelines outlining the dependence of the heliostat loads on the turbulence flow characteristics with varying surface roughness of terrain surrounding a heliostat field site.

ACKNOWLEDGMENTS

The authors would like to acknowledge the financial support for the work, provided by the Australian Government Research Training Program Scholarship, and by the Australian Solar Thermal Research Institute (ASTRI) through funding provided by the Australian Renewable Energy Agency (ARENA).

REFERENCES

1. J. A. Peterka and R. G. Derickson, Sandia National Laboratories, Albuquerque, New Mexico, 1992.
2. A. Jafari, F. Ghanadi, M. Arjomandi, M. J. Emes and B. S. Cazzolato, Journal of Wind Engineering and Industrial Aerodynamics, **189**, 218-230 (2019a).
3. C. K. Ho, D. Griffith, J. N. I. Sment, A. C. Moya and P. Hunter, Dynamic Testing and Analysis of Heliostats to Evaluate Impacts of Wind on Optical Performance and Structural Fatigue (Presentation), in: SolarPACES, Sandia National Laboratories, Marrakech, Morocco, 2012.
4. A. Pfahl, A. Brucks and C. Holze, Energy Procedia, **49**, 193-200 (2014).
5. ASCE 7-02, Minimum design wind loads for buildings and other structures, (American Society of Civil Engineers, Reston, Virginia, 2002).
6. AS/NZS 1170.2, Standards Australia and Standards New Zealand, Sydney, 2011.
7. ASCE/SEI 7-16, American Society of Civil Engineers, Reston, Virginia, 2016.
8. ESDU 85020, Characteristics of atmospheric turbulence near the ground, Part II: single point data for strong winds (neutral atmosphere), (Engineering Sciences Data Unit, London, 2001).
9. M. J. Emes, M. Arjomandi, F. Ghanadi and R. M. Kelso, Solar Energy, **157**, 284-297 (2017).
10. A. Jafari, F. Ghanadi, M. J. Emes, M. Arjomandi and B. S. Cazzolato, Journal of Wind Engineering and Industrial Aerodynamics, **193**, 103955 (2019b).
11. M. J. Emes, A. Jafari, F. Ghanadi and M. Arjomandi, "A method for the calculation of the design wind loads on heliostats," in *SolarPACES*, (AIP Conference Proceedings, Casablanca, Morocco, 2019).
12. E. Simiu and R. H. Scanlan, Wind effects on structures: fundamentals and applications to design, John Wiley & Sons, 1996.
13. M. J. Emes, A. Jafari, F. Ghanadi and M. Arjomandi, Solar Energy (under review).
14. J. A. Peterka, Z. Tan, J. E. Cermak and B. Bienkiewicz, Journal of Solar Energy Engineering, **111**, 158-164 (1989).
15. A. Pfahl, M. Randt, F. Meier, M. Zaschke, C. Geurts and M. Buselmeier, Energy Procedia, **69**, 178-187 (2015).
16. B. Gong, Z. Li, Z. Wang and Y. Wang, Renewable Energy, **38**, 206-213 (2012).
17. D. T. Griffith, A. C. Moya, C. K. Ho and P. S. Hunter, Journal of Solar Energy Engineering, **137**, 021010 (2015).
18. J. A. Peterka, Z. Tan, B. Bienkiewicz and J. Cermak, Solar Energy Research Institute, Golden, Colorado, 1988.
19. J. Vásquez-Arango, "Dynamic Wind Loads on Heliostats", Ph.D. thesis, PhD Thesis, DLR, Uni Aachen, 2016.
20. C. K. Ho, D. T. Griffith, J. Sment, A. C. Moya, J. M. Christian, J. K. Yuan and P. S. Hunter, Dynamic Testing and Analysis of Heliostats to Evaluate Impacts of Wind on Optical Performance and Structural Fatigue, in: SolarPACES, AIP Conference Proceedings, Marrakech, Morocco, 2012, 22695.